

# ***FUSE* Observations of the Loop I/Local Bubble Interaction Region<sup>1</sup>**

Shauna M. Sallmen

Department of Physics, University of Wisconsin - La Crosse, La Crosse, WI 54601

sallmen.shau@uwlax.edu

Eric J. Korpela

Space Sciences Laboratory, University of California at Berkeley, Berkeley, CA, 94720

Hiroki Yamashita

Department of Physics, McGill University, Montreal, QC, Canada, H3A 2T8

Received \_\_\_\_\_; accepted \_\_\_\_\_

---

<sup>1</sup>Based on observations made with the NASA-CNES-CSA Far Ultraviolet Spectroscopic Explorer. FUSE is operated for NASA by the Johns Hopkins University under NASA contract NAS5-32985.

## ABSTRACT

We used the *FUSE* (*Far Ultraviolet Spectroscopic Explorer*) satellite to observe O VI emission along two sightlines towards the edge of the interaction zone (IZ) between the Loop I superbubble and the Local Bubble. One sightline was chosen because material in the interaction zone blocks distant X-ray emission, and should thus do the same for non-local O VI emission. We measured an O VI intensity of  $I_{\text{shadowed}} = 2750 \pm 550$  photons  $\text{cm}^{-2} \text{s}^{-1} \text{sr}^{-1}$  along this ‘Shadowed’ sightline, and  $I_{\text{unshadowed}} = 10800 \pm 1200$  photons  $\text{cm}^{-2} \text{s}^{-1} \text{sr}^{-1}$  along the other sightline. Given these results, very little ( $\lesssim 800$  photons  $\text{cm}^{-2} \text{s}^{-1} \text{sr}^{-1}$ ) of the emission arises from the near side of the interaction zone, which likely has an H I column density of about  $4 \times 10^{20} \text{cm}^{-2}$  along the ‘Shadowed’ sightline. The O VI emission arising within Loop I ( $\sim 10^4$  photons  $\text{cm}^{-2} \text{s}^{-1} \text{sr}^{-1}$ ) is probably associated with gas of  $n_e \sim 0.1 \text{cm}^{-3}$  and an emitting pathlength of  $\sim 1.2$  pc, suggesting it arises at interfaces rather than from gas filling Loop I. In contrast, the C III emission is similar along both sightlines, indicating that much of the emission likely arises on the near side of the interaction zone.

*Subject headings:* ISM: general — ISM: bubbles, ISM: supernova remnants, ISM: individual(Loop I), ultraviolet: ISM

## 1. Introduction

Gas in the galactic interstellar medium (ISM), including the galactic halo, is heated by energy input from stellar winds and supernova events. These processes are responsible for redistributing energy and material throughout our galaxy, resulting in the formation of new generations of stars. The non-uniform interstellar gas exhibits a complex set of interacting shells, bubble-like structures, “chimneys”, and worms that are seen as evidence of stellar energy input. Although the physical state and evolution of these gas phases have been broadly explained, it has not yet been determined whether the ISM is best described by a three-phase model (McKee & Ostriker 1977), a galactic fountain model (Shapiro & Field 1976), or a model with more isolated supernova remnants (Cox & Smith 1974; Slavin & Cox 1993). There are still many outstanding problems with these (and all other current) models of the ISM.

The far-UV (900-1200Å) spectrum of diffuse interstellar emission contains astrophysically important cooling lines: The O VI doublet ( $\lambda\lambda 1032, 1038$ ) represents the dominant radiative cooling mechanism for gas with temperatures between  $10^{5.4}$  and  $10^{5.7}$  K. The C III line ( $\lambda 977$ ) is an important cooling mechanism in gas with temperatures between  $10^{4.5}$  and  $10^{5.1}$  K (Young et al. 2003). Because of the high cooling rates due to these and other lines, gas in this temperature range cools rapidly to lower temperatures, and therefore we refer to gas in this temperature range as “transition temperature gas”. Due to the rapid cooling, in order to be observed this gas must be replenished, either from a source of higher temperature gas cooling through this temperature range, shock heating of cooler gas, conductive heating in a boundary between hot and cold gas, or turbulent mixing of hot and cold gas (McKee & Ostriker 1977; Spitzer 1990; Slavin et al. 1993).

The O VI ion, characteristic of gas with a temperature of  $\sim 300,000$  K, is a sensitive probe of transition temperature gas in our galaxy. In recent years, several detections of

galactic O VI emission have been made with the *FUSE* (*Far Ultraviolet Spectroscopic Explorer*) satellite. Typical values at 1032 Å in directions with low  $N(\text{H I})$  are 2000-3300 photons  $\text{cm}^{-2} \text{s}^{-1} \text{sr}^{-1}$  (LU) (Dixon et al. 2001; Shelton et al. 2001; Shelton 2002, 2003; Welsh et al. 2002), although a recent measurement of halo gas was somewhat higher (Shelton et al. 2007). The O VI survey of Dixon et al. (2006) sampled 183 sightlines, 29 at  $3\text{-}\sigma$  significance, with a median of 3300 LU. The median value of all  $3\text{-}\sigma$  upper limits is 2600 LU. Until recently, the galactic location of this hot-gas emission was unknown. Shelton (2003) concludes that the local ( $< 230$  pc) contribution to this emission is negligible, with a  $2\text{-}\sigma$  upper limit of 500 LU in the direction  $(l,b) = (278.6^\circ, -45.3^\circ)$  (later revised to 600 LU by Dixon et al. (2006)). It therefore appears likely that most emission at high galactic latitudes arises from hot gas in the galactic halo.

Superbubbles are extremely large structures in the ISM, believed to be blown by the combined energy output of a cluster of stars. Such regions provide an important diagnostic of the processes by which supernovae and stellar winds control the overall evolution of our galaxy. Superbubbles are expected to be filled with hot emitting gas. O VI emission intensities towards supernova remnants (SNRs) and superbubbles can be significantly higher than in the general ISM. Dixon et al. (2006) noted two sightlines in their survey that fit this category, each with OVI intensities exceeding 8000 LU. *SPEAR* detected the extremely high value of 180,000 LU towards the Vela SNR (Nishikida et al. 2006), and nearly 7000 LU towards the edge of the Orion-Eridanus Superbubble (Kregenow et al. 2006).

In this paper, a shadowing strategy is used to determine the location of hot emitting gas towards the Loop I superbubble. Observations for the adjacent directions were made to compare the intensity of emission from each sightline. Since one sightline contains material which significantly blocks the distant emission and the other does not, intensities from each sightline are different. This difference in intensity tells us the general location of hot

emitting gas.

In Subsection 1.1, we outline the important characteristics of the region of our observations. Sections 2 and 3 describe the observations and results. In Section 4 we discuss what our observations tell us about physical conditions in the Loop I superbubble and the Local Bubble.

### 1.1. Description of Region

Loop I is a large-scale structure first discovered in the radio continuum sky (Berkhuijsen et al. 1971). The  $116^\circ \pm 4^\circ$  radio ring is centered on  $(l,b) = (329^\circ \pm 1.5^\circ, 17.5^\circ \pm 3^\circ)$ . It is widely believed to be a superbubble blown by strong stellar winds and supernovae of the Sco-Cen OB association ( $\sim 170$  pc away). X-ray, neutral hydrogen, and optical absorption measurements are consistent with a shell of radius  $\sim 100$  pc centered  $\sim 130$  pc away in the direction  $(l,b) = (330^\circ, 15^\circ)$ , with the receding shell  $\lesssim 212$  pc away (Nishikida 1999). Note, however, that Welsh & Lallement (2005) used *HST-STIS* UV absorption spectra towards the approximate center of Loop I,  $(l,b) = (330^\circ, 18^\circ)$ , and estimated that the approaching and receding walls of Loop I are about 90 pc and 150-180 pc, respectively.

Egger & Aschenbach (1995) identified an annular structure (see Figure 3 of their paper) seen inside the Loop I neutral-hydrogen shell in the H I map of Dickey & Lockman (1990). This feature is interpreted as the interaction zone (IZ) between Loop I and our Local Bubble. Using data compiled by Fruscione et al. (1994), Egger & Aschenbach (1995) determined that its distance is  $\sim 70$  pc and  $N_H$  jumps from less than  $10^{20}$  cm $^{-2}$  to over  $7 \times 10^{20}$  cm $^{-2}$  at this distance. If Loop I is spherical, this distance is inconsistent with the aforementioned results of Welsh & Lallement (2005). However, Corradi et al. (2003) used

color excesses to indicate that the interaction zone is twisted and folded, with a transition to higher reddening values occurring at distances ranging from 60 pc to 180 pc, depending on direction, a result further supported by absorption-line studies of the region interior to the annulus (Corradi et al. 2004).

Our observations lie along the edge of the IZ near  $(l,b) = (277^\circ, +9^\circ)$ . The  $\frac{1}{4}$  keV X-ray map for a small region surrounding our observations is shown in Figure 1 (Snowden et al. 1997). The ‘Shadowed’ sightline intersects the neutral-hydrogen interaction zone, while the ‘Unshadowed’ sightline passes through an adjacent region of low neutral-hydrogen column density. The neutral gas blocks high-energy photons, causing the X-ray shadowing effect seen in the *ROSAT* image. This same material will block distant O VI emission. Comparison of the two sightlines gives us the opportunity to distinguish between local and distant emission.

Figure 2 schematically shows the Local Bubble, Loop I superbubble, and the interaction zone between them. The lines of sight are shown for each direction of observation.

## 2. Observations

*FUSE* is composed of four separate optical systems. Two employ LiF optical coatings and are sensitive to wavelengths from 990 to 1187 Å, while the other two use SiC coatings, which provide reflectivity to wavelengths as short as 905 Å. The four channels overlap in the astrophysically important 990-1070 Å region. For a complete description of *FUSE*, its mission, and its in-flight performance, see Moos et al. (2000) and Sahnou et al. (2000).

The *FUSE* spectrum of the ‘Shadowed’ sightline was obtained in 3 observations (C1640401, C1640402, C1640403). The first two were obtained on 2002 June 27-29, and the

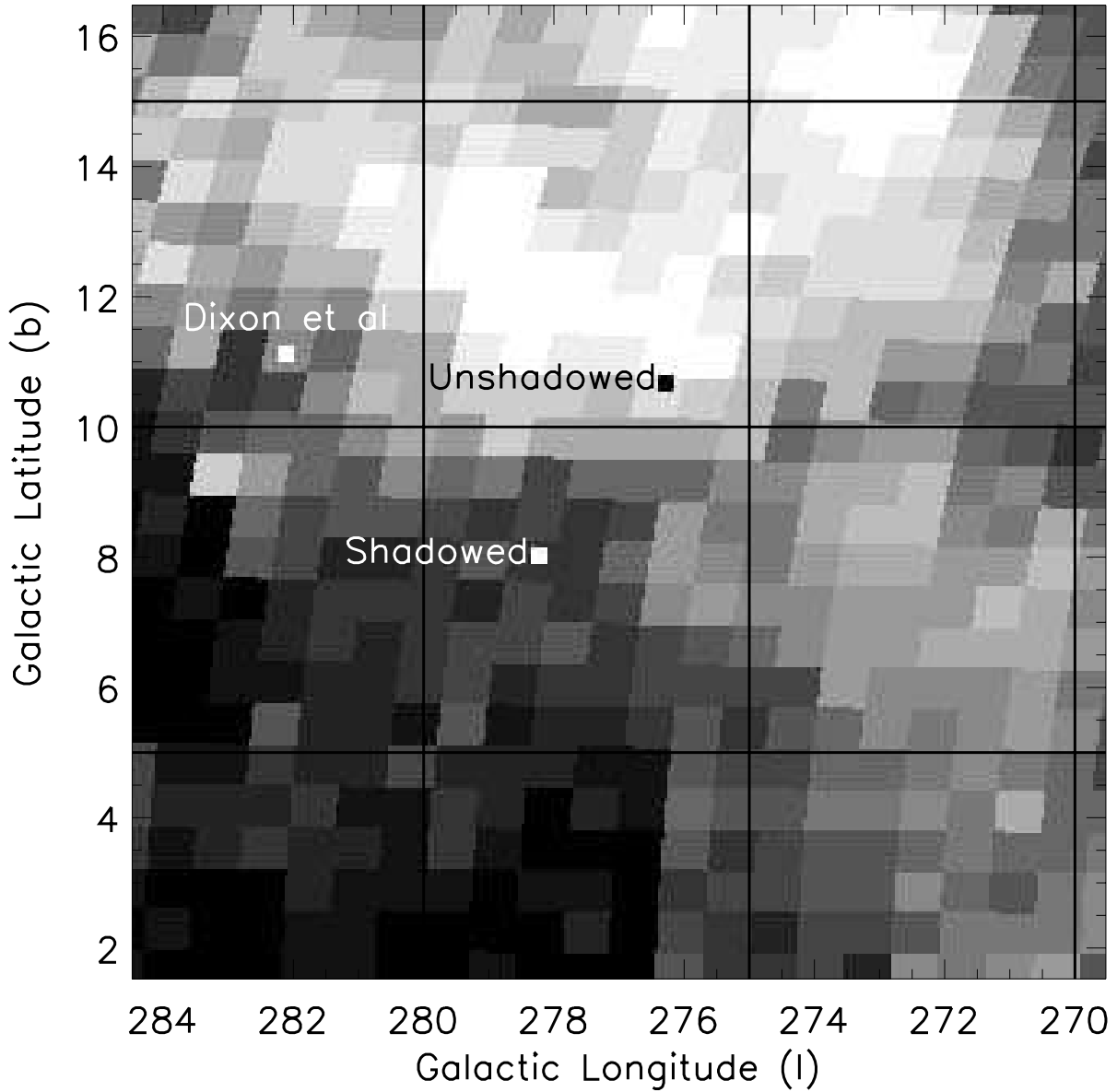


Fig. 1.— 1/4 keV *ROSAT* map (Snowden et al. 1997) showing our sightlines, as well as the location of an O VI detection by Dixon et al. (2006). More X-rays are received from brighter areas. Note the X-ray shadowing due to the neutral hydrogen in the IZ.

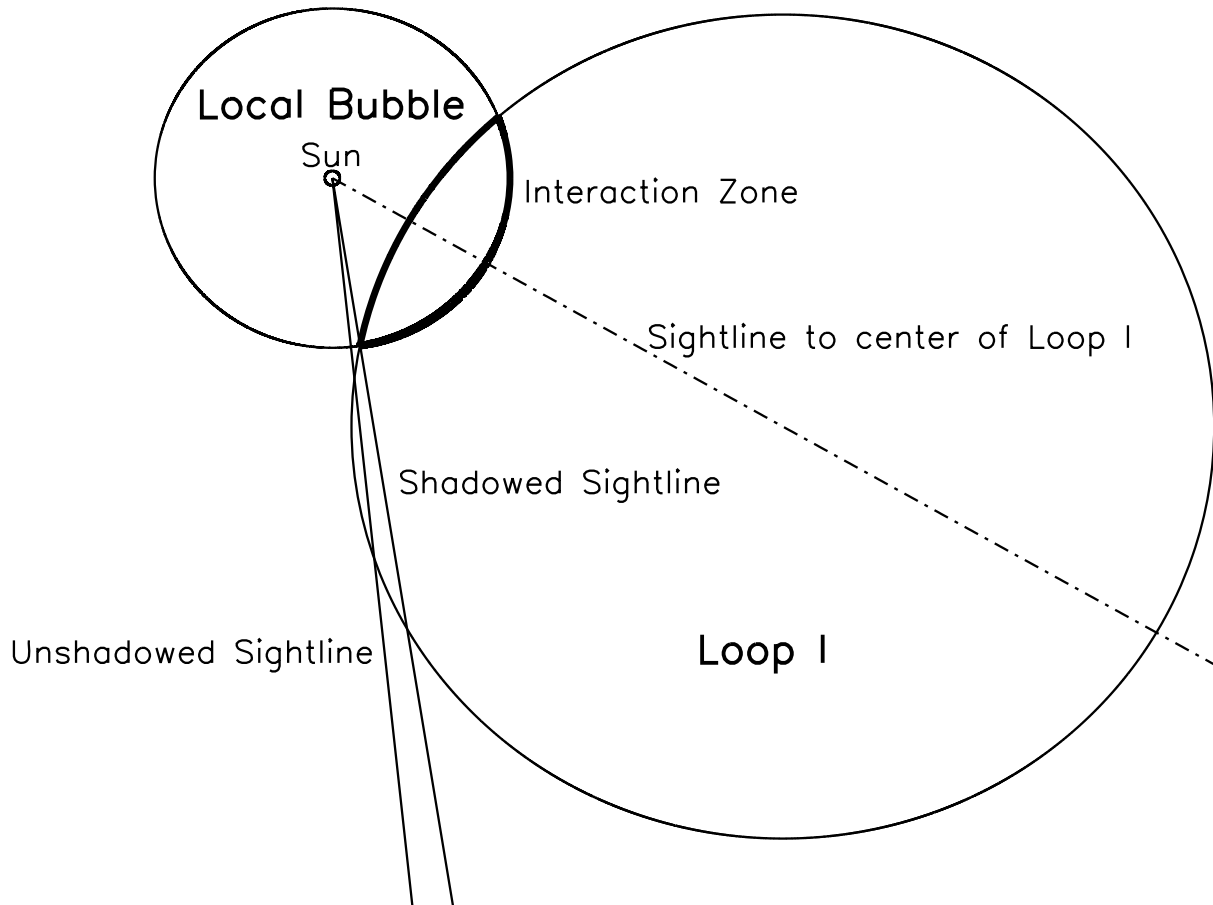


Fig. 2.— Schematic Diagram showing the relative locations of the Sun, Local Bubble, Loop I Superbubble, interaction zone, and our sightlines.



third on 2003 February 18/19. Each exposure was centered on  $(l,b) = (278.23^\circ, +8.02^\circ)$ . The total usable exposure time for detector 1 was (after screening by the pipeline) about 60 ksec, with 40.6 ksec obtained in orbital night. Detector 2 had an additional 24.5 ksec of usable data, of which 4.4 ksec were obtained in orbital night. Data for the ‘Unshadowed’ sightline (C1640301), centered on  $(l,b) = (276.26^\circ, +10.692^\circ)$ , were obtained on 2004 April 3/4. The total usable exposure time for both detectors was about 43 ksec, with 30 ksec obtained during orbital night.

Data were reduced using CalFUSE v3.1.3. The data reduction process includes burst screening, removal of data obtained during passages through the South Atlantic Anomaly or at low earth-limb angles, pulse height screening, corrections for spacecraft motions, dead-time corrections, and spectral binning to  $0.013 \text{ \AA}$  (Dixon et al. 2007). The pipeline also performs an initial wavelength calibration, as well as flux calibration. Background removal was suppressed. After testing, default pulse height ranges were deemed appropriate and used for all detector segments.

The exposures for each observation were added together prior to final spectral extraction. In addition, all data were processed once including photons from both orbital day and orbital night, and once including only those from orbital night. For SiC channels, scattered sunlight contaminates the daytime spectra, so only orbital night spectra were used.

For each detector segment / optical channel, we determined the zero point of the wavelength scale by measuring the observed heliocentric wavelengths of airglow lines for each observation, and applying the measured offset (no other term was deemed necessary) to the spectrum. After this, multiple observations were combined on this corrected heliocentric scale, if necessary. This should correct for possible velocity shifts between the various segments. Remaining systematic errors in wavelength are estimated to be  $\sim 15 \text{ km s}^{-1}$  for

LiF 1a, LiF 2a, and SiC 2a (corresponding to 0.052 Å for LiF 1a). We were unable to accurately wavelength calibrate the SiC 1a spectrum.

### 3. Spectral Analysis and Results

The resulting spectra for the two sightlines are shown for the 1030-1040Å wavelength region in Figure 3. Only nighttime spectra are shown, as several others have noted an apparent airglow feature (possibly the second-order diffraction peak of He I at 515.62Å) near 1032 Å (Welsh et al. 2002; Shelton et al. 2007). No such feature is detectable in our data, and the nighttime measurements are entirely consistent with spectra produced by including daytime data. The two emission lines of the O VI doublet are clearly visible. The 1038 Å line is blended with a 1037 Å C II\* emission line. The intensities of these lines were measured as follows.

Each emission line was assumed to be described by a 106 km s<sup>-1</sup> tophat (image of LWRs aperture) convolved with a Gaussian characterized by  $\sigma_G$ , which includes both intrinsic and instrumental contributions (Dixon et al. 2006). The 106 km/s appears to be nearly correct for LiF1a, but the airglow lines appear somewhat narrower for other detector segments. The data were binned by 4 pixels prior to fitting, resulting in a pixel scale corresponding to 15 km/s. The errors were also smoothed so as to avoid 0 values, without removing significant structure. The lines were fit using the IDL-based MPFIT routines developed by Craig Markwardt<sup>1</sup>. Initially, only the 1032 Å line was included in the fit. Since the C II\* emission line at 1037 Å is mixed with O VI emission at 1038 Å, we assume that the 1038 Å O VI emission line is half the intensity of the O VI emission line at 1032 Å. This assumption is true for optically thin gas, and yields reasonable results in this case.

---

<sup>1</sup><http://cow.physics.wisc.edu/~craigm/idl/idl.html>

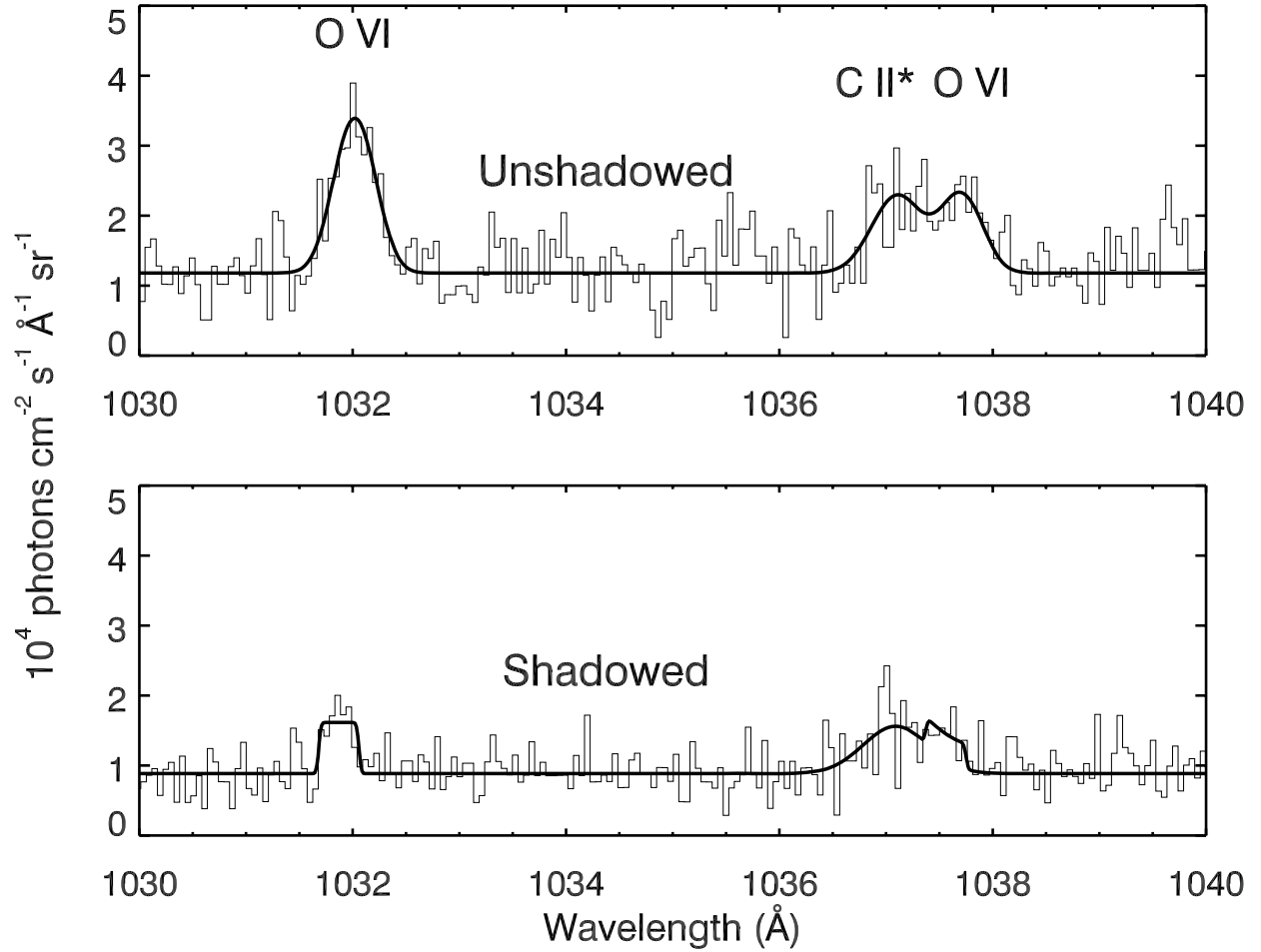


Fig. 3.— Night-only O VI spectrum for the two sightlines. Spectral data have been binned to  $0.052 \text{ \AA}$ . The dark solid line represents our fitted model, as described in the text.

This O VI fitted model was removed from the entire spectrum, leaving the C II\* emission line. The C II\* emission line was then fitted in the same way as the O VI emission line. The reasonableness of the C II\* fits validates this procedure. The complete model is shown over the original spectrum in the figure.

The results of the O VI fits are reported in Table 1. The results of the C II\* fits are included in Table 2. The heliocentric wavelengths yield a heliocentric radial velocity, and have been converted to the standard Local Standard of Rest (LSR) in Table 1. The  $1\text{-}\sigma$  random error bars for each model parameter have been determined using the error estimation prescription of Press et al. (1988), as described in Dixon et al. (2001). Note that the flux calibration uncertainty of  $\sim 10\%$  (Sahnow et al. 2000), when combined with uncertainty in the solid angle of the LWRS aperture, results in a systematic uncertainty of  $\sim 14\%$  (Shelton et al. 2001). The width of the convolving Gaussian (reported as  $\sigma_G$  in Table 1) includes both the intrinsic width of the emission line, and an instrumental contribution of 25 km/s (Dixon et al. 2006). The FWHM reported in Table 1 have been adjusted for this instrumental effect, without associating any error with the correction.

As noted earlier, we see no sign of contamination by airglow in the full dataset. However, in what follows we restrict ourselves to the results from the night-only spectra. In general, measurements from the full dataset are similar to those from the night-only spectra.

We also searched all the night-only spectra for any other detections at the  $\sim 3\sigma$  level. For every wavelength region, we considered the detector segment with the highest effective area. We assumed that the instrumental response was a tophat with width  $0.365\text{\AA}$  (corresponding to  $106\text{ km s}^{-1}$  at  $1032\text{\AA}$ ). We took a running average of each spectrum using this width, adjusting the errors appropriately. After removing a local median estimate of the continuum / background for each point, we statistically determined the 99.7% confidence

limit of the data. Since the errors are likely underestimated due to the low number of counts, this does not correspond precisely to a  $3\sigma$  level. Any spectral data points exceeding this level (often airglow) were investigated, and the results for all spectra/detectors at that wavelength were compared. Line-fitting and error determination was done (as described earlier) for both sightlines if warranted for either. In some cases we excluded lines which appeared to be marginal detections in low sensitivity spectra, but did not appear in higher sensitivity spectra taken with other detector segments. The results of the fits are reported in Table 2, including the LSR radial velocity for features detected on both sightlines.

Note that we have searched for features that result from a filled (or nearly filled) aperture, but minimal intrinsic width. We might therefore have missed significant broad features in the spectra. As an example, consider the C III line, which met our criteria in the ‘Shadowed’ sightline but not the ‘Unshadowed’ one, where it is broader (see Table 2).

To determine upper limits on astrophysically interesting emission lines, we first estimated the 95% confidence limit for each point, evaluated in the same fashion as discussed above. We then determined the median value of this limit in a region  $0.5 \text{ \AA}$  wide. These values are quoted in Table 2. Any feature for which some points lay above the 95% confidence level in this region were fit. The results of the fits are included in the table, however the widths were poorly determined and are not tabulated. From these measurements, we tabulate the radial LSR velocity only for intensity measurements that are unlikely to be contaminated with airglow.

## 4. Discussion

### 4.1. O VI Intensities within Loop I

The observed intensities for the ‘Shadowed’ and ‘Unshadowed’ sightlines are  $I_{\text{shadowed}} = 2750 \pm 550$  photons  $\text{cm}^{-2} \text{s}^{-1} \text{sr}^{-1}$  and  $I_{\text{unshadowed}} = 10800 \pm 1200$  photons  $\text{cm}^{-2} \text{s}^{-1} \text{sr}^{-1}$  (LU). To interpret our data, we made several assumptions and used the following two equations for the intensity of emission from each sightline:

$$I_{\text{shadowed}} = I_{\text{LB}} + I_{\text{beyond}} e^{-\tau_s}$$

$$I_{\text{unshadowed}} = I_{\text{LB}} + I_{\text{beyond}} e^{-\tau_{us}}$$

where  $I_{\text{LB}}$  indicates the intensity of emission from the Local Bubble (more specifically, from the near side of the IZ) and  $I_{\text{beyond}}$  indicates the intensity of emission from beyond any intervening material along the ‘Unshadowed’ sightline. This material has optical depth  $\tau_s$  along the ‘Shadowed’ sightline and  $\tau_{us}$  along the ‘Unshadowed’ sightline. Note that  $\tau_{us}$  may be non-zero, because that sightline passes through the boundaries of both the Local Bubble and Loop I (see Figure 2). Most significantly, we are assuming that  $I_{\text{LB}}$  and  $I_{\text{beyond}}$  are the same along both the ‘Shadowed’ and ‘Unshadowed’ sightlines, and that the difference between the optical depths along the two sightlines ( $\tau_{\text{IZ}}$ ) is due entirely to material in the IZ. It is unclear how patchy the O VI emission or absorbing material might be. The possible limitations of these simplifying assumptions must be kept in mind throughout the discussion below.

Because we expect the IZ to contain most of the absorbing material, for simplicity in this section we assume that  $\tau_{us} = 0$  and  $\tau_s = \tau_{\text{IZ}} = \tau$ . We will relax this assumption in Section 4.2. To get a lower limit on the O VI emission interior to Loop I, we assumed (Case 1) that the interaction zone (IZ) was completely opaque ( $\tau = \infty$ ). In this case,  $I_{\text{LB}} = 2750$

$\pm 550$  LU and  $I_{\text{beyond}} = 8050 \pm 1320$  LU. In Case 2, we assumed that no emission arose within the Local Bubble ( $I_{\text{LB}} = 0$  LU), reflecting the results of Shelton (2003). This yields  $I_{\text{beyond}} = 10800 \pm 1200$  LU, optical depth  $\tau = 1.4 \pm 0.2$  and  $N(\text{H I})_{\text{IZ}} = 4.1 \pm 0.7 \times 10^{20} \text{ cm}^{-2}$  (assuming  $N(\text{H I}) = 3 \times 10^{20} \text{ cm}^{-2}$  for  $\tau = 1$ ; Sasseen et al. (2002)). Finally, for Case 3 we assumed that the shadowing material in this region had the average properties of the interaction zone as determined by Egger & Aschenbach (1995). Under these assumptions  $N(\text{H I})_{\text{IZ}} = 7 \times 10^{20} \text{ cm}^{-2}$ ,  $\tau = 2.3$ ,  $I_{\text{LB}} = 1890 \pm 620$  LU and  $I_{\text{beyond}} = 8910 \pm 1460$  LU.

The extreme Case 1 is unlikely to be correct, especially in light of the Shelton (2003) upper limit to Local Bubble emission of 600 LU (revised by Dixon et al. (2006)), but the derived lower limit does indicate that substantial emission must be arising from beyond the IZ. Case 2 provides a lower limit on the IZ H I column density that is consistent with our results and assumptions, since a smaller value for  $N(\text{H I})$  yields negative emission within the Local Bubble. Note that assuming the Local Bubble contribution is  $I_{\text{LB}} = 600$  LU does not significantly change the calculated value of  $\tau$  or  $N(\text{H I})_{\text{IZ}}$  for this Case. The Local Bubble contribution resulting from Case 3 is significantly larger than the Shelton (2003) upper limit. Either the actual H I column density of the IZ along our sightline is less than the value reported by Egger & Aschenbach (1995), the Local Bubble O VI emission is substantially non-uniform, or there is more O VI emission arising in interfaces on the near side of the IZ than elsewhere in the Local Bubble. In the latter case, the interaction between Loop I and the Local Bubble may have compressed or otherwise altered Local Bubble material in this region. As we will discuss below and in Section 4.2, the Case 3 H I column density is also inconsistent with other estimates of  $N(\text{H I})_{\text{IZ}}$ .

Recent data from Reis & Corradi (2007, personal communication) suggest that the interaction zone along this line of sight has an  $E(b - y)$  extinction of 0.03, which would be equivalent to a hydrogen column of  $\sim 2 \times 10^{20} \text{ cm}^{-2}$  (Knude 1978). This is a factor of two

below the lower limit to H I column density consistent with our simple model (see Case 2 above), and appears inconsistent with our results and assumptions. However, since our particular line of sight was chosen because of a notable X-ray shadow, it is likely that it represents a more dense portion of the interaction zone than is typical, and so has a higher column density than is typical.

We also considered the Dickey & Lockman (1990) measurements of total (to infinite distance) H I column density along the line of sight for both sightlines. The nearest Dickey & Lockman (hereafter DL) measurements give  $N(\text{H I})_{unsh} = 1.259 \times 10^{21} \text{ cm}^{-2}$  and  $N(\text{H I})_{shad} = 1.412 \times 10^{21} \text{ cm}^{-2}$ . The difference between them is  $1.53 \times 10^{20} \text{ cm}^{-2}$ , which we use to estimate  $\tau$ , assuming that this difference arises solely within the IZ. Then our simple model yields an unphysical negative value for the Local Bubble intensity, suggesting that the total neutral hydrogen differences in the two directions are not due only to the interaction zone, but also include differences in material beyond the IZ; we cannot necessarily use these measurements to estimate  $\tau_{IZ}$ . Interpolating over the four nearest DL measurements<sup>2</sup> gives  $N(\text{H I})_{unsh} = 1.018 \times 10^{21} \text{ cm}^{-2}$  and  $N(\text{H I})_{shad} = 1.416 \times 10^{21} \text{ cm}^{-2}$ . The difference between these is  $3.97 \times 10^{20} \text{ cm}^{-2}$ , consistent with Case 2 above. However, because DL is a composite of multiple surveys averaged over 1 degree bins and because galactic column densities can vary significantly over arcminute scales, there are potentially large errors when comparing to emission in two 30'' fields.

Dixon et al. (2006) detected O VI emission with an intensity of  $4000 \pm 1300 \text{ LU}$  along a nearby sightline at  $(l,b) = (282.1^\circ, +11.1^\circ)$ . As can be seen in Figure 1, this sightline also lies near the edge of the IZ, and has less extinction at  $\frac{1}{4} \text{ keV}$  than our ‘Shadowed’ sightline, but more than our ‘Unshadowed’ sightline. Not surprisingly, the observed O VI emission

---

<sup>2</sup>Retrieved using *CHANDRA*’s Colden Neutral Hydrogen Density Calculator at <http://cxc.harvard.edu/toolkit/colden.jsp>



lies between our two measurements. However, the  $1\text{-}\sigma$  errors are such that this sightline could, in principle, have O VI emission less than that along our ‘Shadowed’ sightline. As a result, this sightline is of limited use in further constraining our results.

In all cases considered, the local contribution to the emission is small, indicating that most of the emission lies beyond our Local Bubble. In Case 2 (which we prefer), the measured O VI emission along the ‘Shadowed’ sightline largely originates beyond the IZ. The estimated intensity of emission from beyond the IZ is significantly larger than the typical measurement ( $\sim 2500$  LU) for directions of low hydrogen column density. Given the total  $N(\text{H I}) \sim 10^{21} \text{ cm}^{-2}$  along our sightlines, O VI emission from the thick-disk or galactic halo would be attenuated by a factor of  $\sim 20$  ( $e^{-3} \sim 0.05$ ). To provide a significant portion of the observed emission, such a component would require intrinsic intensities of  $10^5$  photons  $\text{cm}^{-2} \text{ s}^{-1} \text{ sr}^{-1}$ , which could only arise from highly over-pressure regions such as young SNR, as seen in O VI maps generated by *SPEAR* (Edelstein et al. (2007), Korpela et al. (2006)). Since no known young SNR exist on this line of sight, we conclude a significant portion of our detected emission must be associated with the Loop I Superbubble itself. For the remainder of the paper, we assume that all detected O VI emission arising beyond the IZ originates within Loop I.

#### 4.2. Physical Conditions within Loop I

It is possible to use the *ROSAT*  $\frac{1}{4}$  keV (R12) and  $\frac{3}{4}$  keV (R34) background measurements to estimate the difference in hydrogen column due to the IZ along each line of sight. Using a  $0.1^\circ$  radius circle centered on our sightlines, the *ROSAT* count rates ( $10^{-6} \text{ counts s}^{-1} \text{ arcmin}^{-2}$ ) along the ‘Shadowed’ sightline are  $R12 = 749 \pm 175$  and  $R34 = 227 \pm 86$  while those for the ‘Unshadowed’ sightline are  $R12 = 1423 \pm 165$  and  $R34$

$= 180 \pm 61$  (Snowden et al. 1997)<sup>3</sup>. We modeled the region as a *CHIANTI* equilibrium plasma model (Dere et al. 1997; Young et al. 2003). The output spectrum of this model is absorbed along the ‘Unshadowed’ line of sight by a non-IZ H I column, and on the other by a combination of the non-IZ H I column and an additional column density due to the IZ. As noted earlier, the boundaries of the Local Bubble and Loop I may well provide material that attenuates emission arising from within Loop I, even along the ‘Unshadowed’ sightline. By assuming that both the X-ray plasma temperature and emission measure are the same on both lines of sight, we use the X-ray band intensities to derive a plasma temperature of  $(1.26 \pm 0.06) \times 10^6$  K, a non-IZ column density of  $(1.5 \pm 0.2) \times 10^{20}$  cm<sup>-2</sup>, and an IZ column density of  $(4.0 \pm 0.2) \times 10^{20}$  cm<sup>-2</sup>. (In this circumstance the errors represent the  $\Delta\chi^2 = 1$  limits of the absorbed plasma models, which includes the statistical errors of the X-ray count rates.) The estimated IZ column density is consistent with the value we obtained for Case 2 by assuming none of our observed O VI emission arises within the Local Bubble, although that result assumed there was no extinction along the ‘Unshadowed’ sightline. The hot X-ray emitting plasma in this model does not produce significant OVI emission ( $I_{OVI} \lesssim 10$  LU) and is, therefore, not sufficient to explain the observed O VI emission without significant additional plasma at lower temperature.

We now relax our earlier assumption that  $\tau_{us} = 0$ , and instead use the values corresponding to the output of the *CHIANTI* models:  $\tau_{us} = 0.50 \pm 0.07$ ,  $\tau_{IZ} = 1.33 \pm 0.07$ , and  $\tau_s = \tau_{us} + \tau_{IZ} = 1.83 \pm 0.09$ . This results in  $I_{beyond} = 18000 \pm 3300$  LU, and  $I_{LB} = -130 \pm 900$  LU. The negative Local Bubble emission is unphysical, but the result is entirely consistent with no emission from this side of the IZ. Based on this model,  $\lesssim 800$  LU (1- $\sigma$  upper limit) of O VI emission arises on the near side of the IZ. Compared with the earlier estimate from Case 2, allowing for extinction by intervening material increases the

---

<sup>3</sup>Retrieved using the X-Ray Background Tool: <http://heasarc.gsfc.nasa.gov/cgi-bin/Tools/xraybg/xrayb>

amount of O VI emission arising within Loop I by  $\sim 60\%$ .

In order to determine how much of the O VI emission arises from hot gas filling the Loop I superbubble, and how much from hot gas mixing with cooler gas at the interfaces within the interaction zone, we estimate the pathlength of the O VI-emitting gas as follows. We first assume that the O VI-emitting plasma is near the temperature of peak O VI emission ( $\sim 3 \times 10^5$  K) and convert the Loop I O VI emission to an emission measure. Using  $18000 \pm 3400$  LU for the extinction corrected Loop I O VI intensity results in an emission measure of  $0.012 \pm 0.002$  cm $^{-6}$  pc. Temperatures away from the O VI peak require higher emission measure, with  $2.4 \times 10^5$  K and  $3.2 \times 10^5$  K representing the points at which the required emission measure would double.

Dixon et al. (2006) found two types of O VI-emitting gas within the galaxy: gas with densities of  $n_e \sim 0.01$  cm $^{-3}$  and gas with  $n_e \sim 0.1$  cm $^{-3}$ . These two densities result in O VI-emitting pathlengths of  $\sim 120$  pc and  $\sim 1.2$  pc, respectively. If we further assume pressure equilibrium between the X-ray emitting plasma and the lower temperature O VI-emitting plasma, as would be expected if the O VI originates in interfaces between hot and cool gas, we can derive the relative filling factors of the X-ray and O VI plasmas within Loop I. We performed this calculation using the appropriate X-ray temperature, X-ray and O VI emission measures as found above. We find that given the above values and their error, the Loop I O VI-emitting path is between 0.71 and 1.2 times the X-ray emitting path if the O VI-emitting plasma is near the O VI peak. If the O VI-emitting plasma is not at the O VI peak, the required path length could be substantially larger. Similarly, if the pressure in the X-ray emitting gas is higher than that of the O VI-emitting gas, the relative O VI-emitting path is correspondingly larger by a factor of  $P_{X-ray}^2/P_{OVI}^2$ . The maximum total X-ray and O VI emitting pathlength through Loop I under the two density assumptions would be either  $\sim 2.5$  pc or  $\sim 250$  pc.

Assuming the distance to the IZ is  $\sim 70$  pc (Egger & Aschenbach 1995), and the radius of the Loop I superbubble is  $\sim 100$  pc (Nishikida 1999), we can use the angular distance between the ‘Unshadowed’ sightline and the center of Loop I (Nishikida 1999) to geometrically determine the distance to the center of Loop I and the pathlength of the ‘Unshadowed’ sightline through Loop I (under the poor assumption of spherical symmetry; see Figure 2). We find that the pathlength along the ‘Unshadowed’ sightline is  $\sim 15$  pc, and the pathlength along the ‘Shadowed’ sightline is  $\sim 20$  pc. Although the exact numbers are sensitive to the choice of input values and geometrical assumptions, the main conclusion is not: since our sightlines do not lie near the center of Loop I, our pathlength through Loop I must be substantially less than its total diameter of  $\sim 200$  pc. As a specific example, if the distance to the IZ is larger than 70 parsecs, then the radius of the (assumed) spherical Loop I must be larger; otherwise our ‘Unshadowed’ sightline lies outside of Loop I (unlikely given the measured O VI intensity in this direction). The resulting inferred pathlength through Loop I would then still be substantially less than the diameter of Loop I. As a result, the density of the O VI-emitting gas is more likely to be  $\sim 0.1$  cm $^{-3}$  (pathlength  $\sim 2.5$  pc) than  $\sim 0.01$  cm $^{-3}$  (pathlength  $\sim 250$  pc). We note that the thermal pressure of 30,000 cm $^{-3}$  K calculated under the assumption of  $n \sim 0.1$  cm $^{-3}$  and  $T \sim 300,000$  K compares well with the Loop I X-ray emitting gas pressure of 46,000 cm $^{-3}$  K estimated by Davelaar et al. (1980) and the midplane X-ray emitting gas pressure of 28,000 cm $^{-3}$  K determined by Snowden et al. (1997). In addition, Figure 2 of Breitschwerdt & de Avillez (2006), who modelled the history and future of the Local and Loop I bubbles, also suggests that the O VI-emitting gas should be confined to the interior interfaces of Loop I.

The intrinsic FWHM of the O VI 1032 Å emission line are reported in Table 1. Since an instrumental contribution of 25 km/s corresponds to a convolving Gaussian with  $\sigma_G = 0.037$  Å any best-fit Gaussian narrower than this indicates that the LWRS aperture is not filled: i.e. that the emitting region is non-uniform. This is technically the case for

our fit to the night-only spectrum along the ‘Shadowed’ sightline, but a filled aperture is within the  $1\text{-}\sigma$  error bars. Under the assumption that the entire intrinsic width is due to thermal broadening, we calculated the temperature of the emitting gas for each of our estimates of O VI intensity. For the night-only ‘Shadowed’ measurement, we assumed a width corresponding to the upper end of the  $1\text{-}\sigma$  error range. This yields a temperature of  $(1.9 \pm 1.4) \times 10^5$  K. The Day + Night ‘Shadowed’ measurement corresponds to a temperature of  $(5.8 \pm 5.8) \times 10^5$  K. The night-only and full-data ‘Unshadowed’ measurements yielded temperatures of  $3.9 \pm 0.15$  million K and  $2.5 \pm 0.15$  million K, respectively. The ‘Shadowed’ measurements are roughly consistent with thermal broadening, while the widths for the ‘Unshadowed’ sightline are larger. This weakly suggests that gas motions, possibly turbulent, are contributing to the width of the O VI emission in Loop I, or that the emission we see comes from more than one distinct emitting region with different radial velocities. As noted earlier, it is likely that the majority of the emission for even the ‘Shadowed’ sightline originates from beyond the IZ. The difference in widths may indicate that the Loop I gas properties differ somewhat between the sightlines. Differences in best-fit radial velocities of the ‘Shadowed’ and ‘Unshadowed’ emission also suggest inhomogeneous properties for the emitting gas within Loop I. It is important to note, however, that non-uniform surface brightness within the 106 km/s wide aperture profile can mimic a velocity shift, and the ‘Shadowed’ sightline width suggests this scenario. This could be due to either inhomogeneous emission or patchy absorption by the IZ.

We note that our derived Loop I O VI emission intensity is much less than that measured by *SPEAR* towards the Vela Supernova Remnant (Nishikida et al. 2006), as is expected since Vela is a much younger structure, containing strong radiative shocks and filled with a large amount of gas cooling through  $\sim 3 \times 10^5$  K. *SPEAR*’s measurement of O VI towards the Orion-Eridanus superbubble is much more similar, peaking at  $\sim 7000$  LU along the edge of the structure, and confined to a region  $\sim 5 - 10$  pc across (Kregenow et al.

2006). Thus the O VI in both Loop I and Orion-Eridanus appears to arise in interfaces at the edge of the bubble, rather than from gas filling the interior.

### 4.3. C III, low-ionization species, and the Local Bubble

The observed C III intensities for the ‘Shadowed’ and ‘Unshadowed’ sightlines are  $I_{\text{shadowed}} = 13300 \pm 2200$  photons  $\text{cm}^{-2} \text{s}^{-1} \text{sr}^{-1}$  and  $I_{\text{unshadowed}} = 15000 \pm 5000$  photons  $\text{cm}^{-2} \text{s}^{-1} \text{sr}^{-1}$ . These measurements are consistent with the  $\sim 10^4$  LU seen by *SPEAR* in this part of the sky (Korpela et al. 2006), although the *SPEAR* measurement is an average over 64 square degrees. We assume that dust opacity at  $977\text{\AA}$  is 13% higher than at  $1032\text{\AA}$  (Sasseen et al. 2002), and use the same optical depth analysis as for the O VI. For the H I column densities from the CHIANTI model of the previous section, we obtain C III intensities of  $12800 \pm 3400$  photons  $\text{cm}^{-2} \text{s}^{-1} \text{sr}^{-1}$  and  $3800_{-3800}^{+12300}$  photons  $\text{cm}^{-2} \text{s}^{-1} \text{sr}^{-1}$  for emission originating on the near and far sides of the IZ, respectively. The large error bars on the distant emission are primarily due to the opacity of the intervening material. The inferred nearby emission is substantially more than the C III observed within the Local Bubble by Shelton (2003), suggesting non-uniform emission, possibly as a result of C III production at inhomogeneous interfaces.

Unlike O VI, a significant proportion of the observed C III emission arises on the near side of the IZ. Of the  $15000 \pm 5000$  photons  $\text{cm}^{-2} \text{s}^{-1} \text{sr}^{-1}$  observed along the ‘Unshadowed’ sightline, at least  $9600$  photons  $\text{cm}^{-2} \text{s}^{-1} \text{sr}^{-1}$  ( $1\text{-}\sigma$  lower limit) arises within the Local Bubble. Such a situation could arise if the interface between the Local Bubble and the interaction zone were significantly cooler ( $\lesssim 10^5 \text{K}$ ) than the Loop I/interaction zone interface, because hot gas within Loop I would further ionize Carbon, reducing the amount of C III emission originating beyond the IZ. This lends support to the idea that the Local Bubble is not filled with overpressured hot ( $10^6 \text{K}$ ) gas (Welsh & Lallement 2005). However,

the large error bars on  $I_{beyond}$  prevent us from concluding that there is no significant C III emission within Loop I.

Three other species, all present in the neutral ISM, have significant measurements along both sightlines: C II\*, Ar I, and Fe II. As may be seen in Table 2, in all cases the measurements for the two sightlines are quite similar, agreeing within the errors. This suggests that most of the emission arises in the near side of the IZ, as for C III. Note that the Ar I measurements may be contaminated by nighttime airglow. The radial velocity for Ar I along the ‘Unshadowed’ sightline is consistent with geocoronal emission at the  $1\text{-}\sigma$  level. Along the ‘Shadowed’ sightline, the Ar I radial velocity is inconsistent with geocoronal emission at the  $1\text{-}\sigma$  (and possibly  $2\text{-}\sigma$ ) level, although it is difficult to be specific since that measurement combines two observations with disparate geocentric to heliocentric corrections. Apart from N II, which may also be contaminated by nighttime airglow, measurements and upper limits for all remaining species in Table 2 are consistent between the two sightlines, again suggesting that emission for these low-ionization species arises largely in the near side of the IZ.

The radial velocities for these species are shown in Table 2. In general, the radial velocities along the ‘Shadowed’ sightline tend to be lower than along the ‘Unshadowed’ sightline, although the relatively large error bars make it difficult to be specific. This could indicate that the emission along the ‘Unshadowed’ sightline arises at the boundary between the Local Bubble and the surrounding neutral ISM, while the emission along the ‘Shadowed’ sightline arises at the interface between the Local Bubble and the interaction zone. In this case, we would expect lower radial velocities along the ‘Shadowed’ sightline, because the expansion of Loop I could push the IZ towards us.

## 5. Conclusions

We have performed a shadowing measurement using absorption of O VI emission along a line of sight that intersects the purported interaction zone between the Loop I superbubble and the Local Bubble. The results are consistent with moderately bright O VI emission ( $\sim 10^4$  photons  $\text{cm}^{-2} \text{s}^{-1} \text{sr}^{-1}$ ) interior to Loop I, likely arising near the walls of the bubble, with absorbing dust in the interaction region equivalent to an H I column density of  $\sim 4 \times 10^{20} \text{cm}^{-2}$ . Less than  $\sim 800$  photons  $\text{cm}^{-2} \text{s}^{-1} \text{sr}^{-1}$  of the observed emission arises from the interface between the Local Bubble and the interaction zone.

Unlike O VI, emission from C III and other low-ionization species along the same sightlines shows a very significant local component. The disparity in the origin of O VI and C III on these sightlines indicates that the conditions in the interface between the interaction region and the Local Bubble are significantly different than in the hot/cold interfaces within Loop I. These differences are likely due to differences in the temperature and pressure of Local Bubble gas relative to conditions within Loop I.

We are grateful to W. Corradi & W. Reis for providing a detailed reddening map of the region near our observations, and K. Nishikida for discussions about Loop I. This paper used observations obtained by the NASA-CNES-CSA *Far Ultraviolet Spectroscopic Explorer* (*FUSE*) mission operated by the Johns Hopkins University, supported by NASA contract NAS5-32985. W.V.D. Dixon was extremely helpful with questions about the *FUSE* pipeline. Funding for this project was provided by NASA through NASA grant NNG05GB62G. We acknowledge the use of NASA's *SkyView* facility (<http://skyview.gsfc.nasa.gov>) located at NASA Goddard Space Flight Center. This research has made use of data obtained from the High Energy Astrophysics Science Archive Research Center (HEASARC), provided by NASA's Goddard Space Flight Center. *CHIANTI* is a collaborative project involving the



NRL (USA), RAL (UK), and the following Universities: College London (UK), Cambridge (UK), George Mason (USA), and Florence (Italy).

Facilities: *FUSE*.

## REFERENCES

- Berkhuijsen, E. M., Haslam, C. G. T., & Salter, C. J. 1971, *A&A*, 14, 252
- Breitschwerdt, D., & de Avillez, M. A. 2006, *A&A*, 452, L1
- Corradi, W. J. B., Franco, G. A. P., & Knude, J. 2004, *MNRAS*, 347, 1065
- Corradi, W. J. B., Guimaraes, M. M., & Vieira, S. L. A. 2003, in *ASP Conf. Ser.* 309, *Astrophysics of Dust*, ed. A. N. Witt, G. C. Clayton, & B. T. Draine (San Francisco: ASP)
- Cox, D. P., & Smith, B. W. 1974, *ApJ*, 189, L105
- Davelaar, J., Bleeker, J. A. M., & Deerenberg, A. J. M. 1980, *A&A*, 92, 231
- Dere, K. P., Landi, E., Mason, H. E., Monsignori Fossi, B. C., & Young, P. R. 1997, *A&AS*, 125, 149
- Dickey, J. M., & Lockman, F. J. 1990, *ARA&A*, 28, 215
- Dixon, W. V. D., Sallmen, S., Hurwitz, M., & Lieu, R. 2001, *ApJ*, 552, L69
- Dixon, W. V. D., Sankrit, R., & Otte, B. 2006, *ApJ*, 647, 328
- Dixon, W. V., et al. 2007, *PASP*, 119, 527
- Edelstein, J., et al. 2007, *American Astronomical Society Meeting Abstracts*, 210, #44.02
- Egger, R. J., & Aschenbach, B. 1995, *A&A*, 294, L25
- Fruscione, A., Hawkins, I., Jelinsky, P., & Wiercigroch, A. 1994, *ApJS*, 94, 127
- Knude, J. 1978, *Astronomical Papers Dedicated to Bengt Stromgren*, 278
- Korpela, E. J., et al. 2006, *Bulletin of the American Astronomical Society*, 38, 919

- Kregenow, J., et al. 2006, ApJ, 644, L167
- McKee, C. F., & Ostriker, J. P. 1977, ApJ, 218, 148
- Moos, H. W., et al. 2000, ApJ, 538, L1
- Nishikida, K. 1999, Ph.D. Thesis, Penn. State
- Nishikida, K., et al. 2006, ApJ, 644, L171
- Press, W. H., Flannery, B. P., Teukolsky, S. A., & Vetterling, W. T. 1988, Numerical Recipes in C: The Art of Scientific Computing, (Cambridge University Press, 1988)
- Reis, W. & Corradi, W. J. B. 2007, A&A, submitted
- Sahnou, D. J., et al. 2000, ApJ, 538, L7
- Sasseen, T. P., et al. 2002, ApJ, 566, 267
- Shapiro, P. R., & Field, G. B. 1976, ApJ, 205, 762
- Shelton, R. L. 2002, ApJ, 569, 758
- Shelton, R. L. 2003, ApJ, 589, 261
- Shelton, R. L., Sallmen, S. M., & Jenkins, E. B. 2007, ApJ, 659, 365
- Shelton, R. L., et al. 2001, ApJ, 560, 730
- Slavin, J. D., & Cox, D. P. 1993, ApJ, 417, 187
- Slavin, J. D., Shull, J. M., & Begelman, M. C. 1993, ApJ, 407, 83
- Snowden, S. L., et al. 1997, ApJ, 485, 125
- Spitzer, L. J. 1990, ARA&A, 28, 71

Welsh, B. Y., & Lallement, R. 2005, *A&A*, 436, 615

Welsh, B. Y., Sallmen, S., Sfeir, D., Shelton, R. L., & Lallement, R. 2002, *A&A*, 394, 691

Young, P. R., Del Zanna, G., Landi, E., Dere, K. P., Mason, H. E., & Landini, M. 2003, *ApJS*, 144, 135

Table 1. 1032 Å O VI Emission

| Sightline               | Data        | O VI intensity<br>(LU <sup>b</sup> ) | $\sigma_G^c$<br>(Å)                    | FWHM <sup>c</sup><br>(km s <sup>-1</sup> ) | V <sub>LSR</sub><br>(km s <sup>-1</sup> ) |
|-------------------------|-------------|--------------------------------------|--|--|---|
| Shadowed <sup>a</sup>   | Night       | 2750 ± 550                           | 0.02 <sup>+0.03</sup> <sub>-0.02</sub> | ≤ 21 <sup>d</sup>                          | −29 ± 6                                   |
| ...                     | Day + Night | 2640 ± 600                           | 0.07 ± 0.06                            | 41 ± 41                                    | −29 ± 10                                  |
| Unshadowed <sup>a</sup> | Night       | 10800 ± 1200                         | 0.16 ± 0.03                            | 107 ± 21                                   | 15 ± 8                                    |
| ...                     | Day + Night | 9580 ± 1000                          | 0.13 ± 0.03                            | 85 ± 21                                    | 16 ± 6                                    |

<sup>a</sup>Shadowed:  $(l, b) = (278.23, +8.02)$ , Unshadowed:  $(l, b) = (276.26, +10.69)$

<sup>b</sup> LU = photons cm<sup>-2</sup> s<sup>-1</sup> sr<sup>-1</sup>

<sup>c</sup>FWHM have been corrected for instrumental contribution, while  $\sigma_G$  have not. Gas at  $T = 3 \times 10^5$  K has a thermal width corresponding to a FWHM of 29 km/s.

<sup>d</sup>The best-fit convolving Gaussian has a FWHM less than the instrumental contribution, suggesting the aperture is not filled, although a filled aperture is within the error bars.

Table 2. Other Emission Lines and Upper Limits

| Species           | Wavelength<br>(Å)    | Detector<br>Segment | SHADOWED                        |                     |                                    | UNSHADOWED        |                     |                                    |
|-------------------|----------------------|---------------------|---------------------------------|---------------------|------------------------------------|-------------------|---------------------|------------------------------------|
|                   |                      |                     | Intensity<br>(LU <sup>b</sup> ) | $\sigma_G^c$<br>(Å) | $V_{LSR}$<br>(km s <sup>-1</sup> ) | Intensity<br>(LU) | $\sigma_G^c$<br>(Å) | $V_{LSR}$<br>(km s <sup>-1</sup> ) |
| C I <sup>a</sup>  | 945.58               | SiC 2a              | 2900 ± 1500                     | ...                 | ...                                | < 8700            | ...                 | ...                                |
| Mg II             | 946.73               | SiC 2a              | 2500 ± 1000                     | ...                 | -26 ± 13                           | <8700             | ...                 | ...                                |
| N I <sup>a</sup>  | 953.97               | SiC 2a              | <4400                           | ...                 | ...                                | <8800             | ...                 | ...                                |
| C III             | 977.02               | SiC 2a              | 13300 ± 2200                    | 0.14 ± 0.04         | -10 ± 10                           | 15000 ± 5000      | 0.29 ± 0.14         | 45 ± 35                            |
| N III             | 991.57               | SiC 2a              | <5300                           | ...                 | ...                                | <10600            | ...                 | ...                                |
| S III             | 1015.55              | LiF 1a              | <1800                           | ...                 | ...                                | <3200             | ...                 | ...                                |
| C II              | 1037.02              | LiF 1a              | 5100 ± 1100                     | 0.28 ± 0.12         | 8 ± 16                             | 6700 ± 1300       | 0.21 ± 0.06         | 13 ± 16                            |
| Ar I <sup>a</sup> | 1048.22              | LiF 1a              | 5000 ± 1100                     | 0.24 ± 0.07         | -61 ± 19                           | 5200 ± 1200       | 0.17 ± 0.06         | -14 ± 16                           |
| S IV              | 1062.66              | LiF 1a              | 1200 ± 800                      | ...                 | 94 ± 45                            | <3300             | ...                 | ...                                |
| S IV              | 1072.99              | LiF 1a              | <2500                           | ...                 | ...                                | <4000             | ...                 | ...                                |
| N II <sup>a</sup> | 1083.99 <sup>d</sup> | SiC 1a              | <12000                          | ...                 | ...                                | 20000 ± 6000      | ...                 | ...                                |
| C I <sup>a</sup>  | 1122.26              | LiF 2a              | <2300                           | ...                 | ...                                | <3400             | ...                 | ...                                |
| Fe III            | 1122.52              | LiF 2a              | <2300                           | ...                 | ...                                | 3100 ± 1400       | ...                 | -17 ± 35                           |
| Fe II             | 1144.94              | LiF 2a              | 2900 ± 800                      | 0.05 ± 0.07         | -26 ± 13                           | 2700 ± 1300       | 0.1 ± 0.1           | 23 ± 22                            |

<sup>a</sup>These lines may contain a contribution due to nighttime airglow

<sup>b</sup> LU = photons cm<sup>-2</sup> s<sup>-1</sup> sr<sup>-1</sup>

<sup>c</sup>The width of the best-fit convolving Gaussian is not included for lines fit only because they exceeded the 95% confidence limit, as these were poorly determined.

<sup>d</sup>Because it was not possible accurately determine the wavelength zero-point of the SiC 1a spectrum, we are unable to determine with certainty which of the NII multiplet lines we observed.